RSC Advances

PAPER

View Article Online
View Journal | View Issue

Cite this: *RSC Adv.*, 2020, **10**, 34690

The electronic structures and magnetic properties of mixed-valence Fe-based metal–organic VNU-15 frameworks: a theoretical study from linear response DFT+U calculations†

Diem Thi-Xuan Dang, *[ab] Hieu Cao Dong,[ab] Yoshiyuki Kawazoe,[cde] Jer-Lai Kuo [f] and Duc Nguyen-Manh [g]

The crystal symmetries, electronic structures, and magnetic properties of metal–organic VNU-15 frameworks (VNU = Vietnam National University) were investigated using density functional calculations (DFT) with an on-site Coulomb repulsion approximation, U_{eff}, of 4.30 eV, determined *via* the linear response method. Two different orientations of dimethylammonium (DMA^+) cations in VNU-15 were investigated. Antiferromagnetic configurations were predicted to be the ground states, with Fe ions in high-spin states for both phases. Furthermore, VNU-15 had intrinsic semiconductor electronic behavior with a small band gap of about 1.20 eV. The change in the orientation of DMA^+ led to changes in the dispersion of the band structure, the band gap, and the Fe contributions to the valence band and conduction band. A fascinating feature was found involving exchange of oxidation numbers between two adjacent Fe atoms in the two phases. Our results revealed that VNU-15 has strong oxidation activity and predicted the important role of an anisotropic effect on the hole and electron effective masses. The findings presented that the electronic and magnetic properties could be controlled *via* hydrogen bonds and proved VNU-15 to be a prospective material for photocatalytic applications.

Received 5th July 2020
Accepted 2nd September 2020

DOI: 10.1039/d0ra05865c

rsc.li/rsc-advances

I. Introduction

Metal or metal-oxide clusters can be combined with organic linkers to create a new class of crystalline material, named metal–organic frameworks (MOFs). These materials have incredible properties, such as high surface areas and porosities, and adjustable physical and chemical properties.[1] For this reason, MOFs have thrived in many application areas, such as catalysis,[2,3] photocatalysis,[4,5] gas storage,[6,7] drug delivery,[8,9] proton transfer,[10,11] and so on. MOF structures, consisting of infinite rod-like secondary building units (SBUs), are useful because of the potential for isoreticular expansion, resistance to interpenetration, and breathing functionality.[12–14] Numerous examples of rod-based SBUs have been reported, but series of solids based on $[M^{II}_3O_3(CO_2)_3]_\infty$ (MOF-74)[15] and $[M^{III}O_2(CO_2)_2]_\infty$ (MIL-53),[16] in which M = Mg, Cr, Fe, Co, *etc.*, have risen to prominence. The II and III indices, relating to a classical chemistry interpretation, indicate the valences of the compounds. These SBUs are composed of hydroxycarboxylate or carboxylate ligands and metal octahedra sharing μ_2–O atoms. Of the numerous metals, Fe rod-based SBUs have been the subject of great interest because of their fascinating electronic and magnetic properties. For instance, Fe–MOF-74 displays ferromagnetic states and dramatically disparate band gaps between majority and minority spins in metastable states.[17] Computational studies have revealed that a high-spin state ($S = 2$) is associated with the Fe ions in this structure.[17–19] Canepa *et al.* investigated the existence of linear magnetism in Fe–MOF-74 at low temperature.[20] The magnetic ordering of nodes of Fe–MOF-74 can be tuned *via* absorbing olefins that coordinate with the transition metal.[18] A large-pore to narrow–pore transition in breathing Fe–MIL-53, resulting in significant alterations of the electronic properties, has been observed.[21] Combelles *et al.* showed that Fe–MIL-53 is a weak anti-ferromagnetic insulator at 0 K, with Fe ions in the high-spin $S = 5/2$ state, through first-principles DFT+U calculations.[22]

Until now, materials containing mixed-valence Fe atoms, such as Fe_3O_4, $Fe^{III}_4[Fe^{II}(CN)_6]_3 \cdot xH_2O$, $[NH_2(CH_3)_2]$

[a]*Center for Innovative Materials and Architectures (INOMAR), Ho Chi Minh City 721337, Vietnam. E-mail: dxdiem@inomar.edu.vn; xuandiemdang@gmail.com*
[b]*Vietnam National University – Ho Chi Minh City, Ho Chi Minh City 721337, Vietnam*
[c]*New Industry Creation Hatchery Center, Tohoku University, Sendai 980-8579, Japan*
[d]*Department of Physics, Suranaree University of Technology, Nakhon Ratchasima, Thailand*
[e]*Department of Physics and Nanotechnology, SRM Institute of Science and Technology, Kattankulathur, Tamil Nadu-603203, India*
[f]*Institute of Atomic and Molecular Sciences, Academia Sinica, Taipei 10617, Taiwan*
[g]*CCFE, United Kingdom Atomic Energy Authority, Culham Science Centre, UK*

† Electronic supplementary information (ESI) available. See DOI: 10.1039/d0ra05865c

$[Fe^{III}Fe^{II}(HCOO)_6]$, *etc.*, have shown outstanding performance in several key applications.[23–25] Nevertheless, the above MOFs are generally constructed from rod chains of octahedral Fe(II) or Fe(III) SBUs from an ionic bonding point of view and, indeed, MOFs composed of mixed-valence Fe(II)- and Fe(III)-based SBUs are scarcely reported in the literature. Recently, Tu *et al.* synthesized VNU-15 (VNU stands for Vietnam National University), formulated as $Fe_4(BDC)_2(NDC)(SO_4)_4(DMA)_4$, where BDC, NDC, and DMA are benzene-1,4-dicarboxylate, naphthalene-2,6-dicarboxylate, and dimethylammonium, respectively. This material is composed of novel infinite rod SBUs $[Fe_2(CO_2)_3(SO_4)_2(DMA)_2]_\infty$ based on both Fe(II) and Fe(III).[26] These SBUs connect with two BDC^{2-} and one NDC^{2-} linker to create VNU-15, which is an anionic MOF balanced electrically with DMA cations. VNU-15 was tested as a proton transfer material in fuel cells and the proton conductivity reached 2.90×10^2 S cm^{-1} at 95 °C and 60% relative humidity. One of the possibilities explaining the high proton conductivity is the formation of a H-bond network between SO_4^{2-} ions and DMA^+ cations through a Grotthuss-type diffusion mechanism.[27] Additionally, the proton conductivity of VNU-15 can be maintained for 40 hours without noticeable loss, and it has good heating–cooling stability.

The outstanding properties of infinite rod MOFs combined with the versatility of Fe have been shown in previous works,[17,18] motivating us to study VNU-15. Although VNU-15 has been synthesized and its structure has been determined *via* X-ray diffraction, little is known about its electronic, magnetic, and other physical properties. Obtaining a comprehensive understanding of the many interesting properties of VNU-15 still remains desirable to provide vital fundamental data for its future utilization. Meanwhile, first-principles density functional calculations have been proven to be powerful in predicting the structural, electronic, and magnetic properties and chemical bonding of a wide series of MOFs.[28,29] In the present work, density functional theory (DFT) with strong-electron correction was used to accurately describe the structure of VNU-15. The electronic structure and magnetic and chemical bonding properties in the ground state of VNU-15 were predicted. Different orientations of DMA cations in the anionic MOF were found to have significant effects on the electronic and magnetic properties of the material.[30] Therefore, in this paper, the influence of the two orientations of DMA cations in VNU-15 on the electronic structures and magnetic properties was also considered.

II. Calculation methods

All theoretical calculations were performed using the DFT method within the Vienna *Ab Initio* simulation package (VASP).[31,32] The generalized gradient approximation (GGA) functional and projector-augmented wave (PAW) method were employed.[33,34] The ion–electron interactions were described using Perdew, Burke, and Ernzerhof (PBE) exchange-correlation.[35] Spin-polarized calculations were performed due to the presence of Fe atoms. van der Waals (vdW) interactions are fundamental in the porous and layered structure of VNU-15; therefore, this work made extensive use of DFT, especially of a functional including the vdW correction D3.[36]

A cut-off energy of 600 eV was identified to provide effective precision based on a cut-off energy study carried out in the range from 300 eV to 800 eV. The absolute energies were converged to within 10^{-5} eV per atom. Fully relaxed optimization of the atomic coordinates of VNU-15 was conducted using the standard conjugate gradient algorithm until the forces on all atoms were less than 10^{-2} eV Å^{-1}. Brillouin-zone integration was performed with a Gaussian broadening of 0.1 eV during all relaxations. In this paper, the PAW treatment of pseudopotentials uses the 3d and 4s electrons for Fe, the 3s and 3p electrons for S, the 2s and 2p electrons for N, C, and O, and the 1 s electron for H. Because of the large primitive cell (approximately 250 atoms per primitive cell), the Γ-point alone was sufficient for sampling the Brillouin zone for all optimization calculations, while a denser $2 \times 2 \times 3$ *k*-point was utilized for the density of states calculations. To understand the chemical bonding and interactions between constituents in VNU-15, charge density difference and Bader charge analyses[37] were performed. The charge density difference was calculated from the subtraction of the electron density of the compound from the electron density of free atoms in the same framework with constant volume. All crystal structures were visualized using the VESTA program.[38]

As the GGA cannot be used to express well systems containing partially filled d-orbitals, the GGA+U method was used.[39] The effective correlation energy, U_{eff}, for Fe d-orbitals was determined *via* a linear response approach:

$$U_{\text{eff}} = \frac{1}{\chi} - \frac{1}{\chi_0}, \tag{1}$$

where χ and χ_0 are the interacting and non-interacting density response coefficients, respectively.[40] These coefficients are respectively defined as shown:

$$\chi = \frac{\partial N_{\text{I}}^{\text{SCF}}}{\partial \alpha_{\text{I}}}, \tag{2}$$

$$\chi_0 = \frac{\partial N_{\text{I}}^{\text{NSCF}}}{\partial \alpha_{\text{I}}}, \tag{3}$$

where N_{I} is the electron occupation of the Fe-3d orbital and α_{I} is the perturbation potential. To determine U_{eff}, the electronic charge density was constructed *via* a self-consistent calculation with vanishing α_{I}. Starting from this initial charge density, the total electronic occupations of the orbital based on non-interacting and self-consistent responses were respectively obtained with several perturbation potentials in a small range (−0.4 to 0.4), which were applied to the Fe 3d-orbitals. In the end, the response function was obtained from the slope of the 3d electron occupation *versus* α_{I},[41] from which the Hubbard U_{eff} term for VNU-15 was determined to be 4.30 eV. The process of determining the U_{eff} value *via* a linear response for DMA-2 was similar to that used for DMA-1, as shown in Fig. 1.

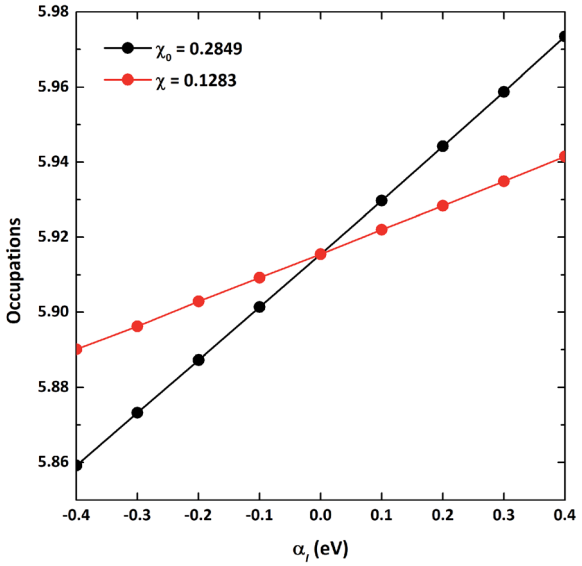

Fig. 1 The total d-orbital electronic occupations with respect to the perturbation potentials (α_i) on the d-orbitals of Fe sites for VNU-15. The non-interacting and self-consistent linear responses are indicated by the black and red circles, respectively.

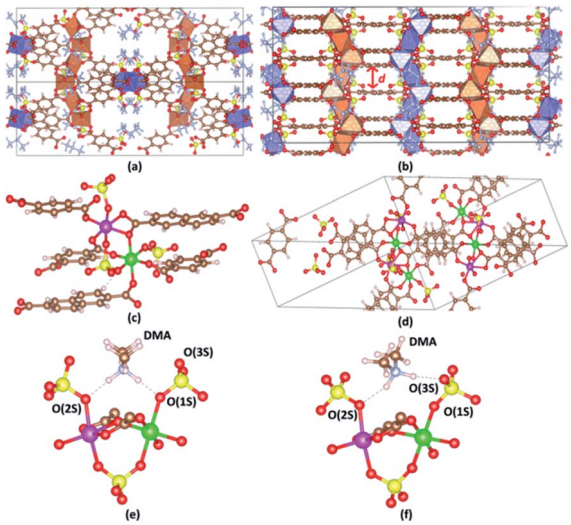

Fig. 2 The single-crystal structure of VNU-15 shown from (a) the [110] and (b) [001] planes, where d (Å) is the interlayer spacing. (c) The coordination environments of the Fe(1) and Fe(2) sites in the VNU-15 structure. (d) Two independent Fe chains with four independent octahedral Fe atoms per chain in the primitive cell. Two different orientations of DMA cations in VNU-15: (e) DMA-1; (f) DMA-2. Atom colors: Fe polyhedrons in (a) and (b), blue and orange; DMA, pale blue; Fe(1), green; Fe(2), pink; C, brown; O, red; S, yellow; H, pale pink. All DMA molecules are omitted for clarity in (c) and (d). O(1S) is the O atom connected between Fe(1) and S, O(2S) is the O atom connected between Fe(2) and S, O(3S) is the O atom only connected with S, O(1C) is the O atom in the BDC^{2-} linker, O(2C) is the O atom in the NDC^{2-} linker. N–H···O–S (1) is the bond between H(DMA) and O(1S) or O(2S). N–H···O–S (2) is the bond between H(DMA) and O(3S) in the DMA-2 phase.

III. Results and discussion

A. The spin configurations and structural properties

The crystal structure of VNU-15 is illustrated in Fig. 2(a and b). The conventional cell of the VNU-15 crystal structure determined from XRD experiments is orthorhombic with the *Fddd* space group (no. 70) and the lattice parameters $a = 16.76$ Å, $b = 18.83$ Å, $c = 39.00$ Å. This cell contains sixteen formula units of $Fe_2(CO_2)_3(SO_4)_2(DMA)_2$ (1088 atoms), while the primitive cell includes four formula units (272 atoms). The experimentally XRD refined crystal structure for VNU-15 includes uncertainties in determining occupancy in different atomic C, H positions in the NDC^{2-} ligand, which is acceptable from crystallographic point of view but creates a major obstacle to applying DFT calculations to VNU-15. The elimination of the disorder can be done manually *via* removing some C and H atoms from the NDC^{2-} linker; then, the conventional cell of the obtained VNU-15 is orthorhombic with the *Fdd*2 space group (no. 43), and the number of atoms in the obtained primitive cell is 244. When analyzing the crystal structure of VNU-15, two distinct metal nodes exist (Fe(1) and Fe(2)), which alternate consecutively in order, as shown in Fig. 2(c). Both Fe(1) and Fe(2) atoms adopt octahedral geometries, with four O atoms at in-plane coordination sites symmetrically comprising two BDC^{2-} linkers and SO_4^{2-} ions. The Fe(1) octahedron has two O atoms from two NDC^{2-} linkers coordinated at the axial sites, whereas the Fe(2) octahedron has two O atoms from one NDC^{2-} linker. For further analysis, calculations on the primitive cell were performed to enable a reduction in research expense and time. This primitive cell contains two independent Fe chains with four independent octahedral Fe atoms per chain (Fig. 2(d)). The relaxed positions of the eight Fe atoms in the primitive cell are shown in Table 1. In the experimental structure,[26] DMA cations are found to orient symmetrically with the infinite rod SBUs because of hydrogen bonding with sulfate ligands (N–H···O–S distances of 1.90–196 Å), as shown in Fig. 2(e), which is denoted as DMA-1. Two hydrogen atoms from DMA are in turn bonded to two oxygen atoms connected between sulfur and iron. Upon optimizing the structure, another orientation of DMA^+ was discovered, as shown in Fig. 2(f), denoted as DMA-2. A hydrogen atom of DMA is bonded to an oxygen atom connected between sulfur and iron, while the other hydrogen of DMA is bonded to an oxygen atom only connected with sulfur. Because both cases are potentially experimental, they are studied in the remainder of this paper.

Investigating various spin configurations may be advantageous for achieving an in-depth understanding of electronic behavior.[42,43] Starting from the non-spin polarized convergence geometries, spin-polarized structure optimizations were carried out as the next step, where the Fe ions were regarded as magnetic centers and distinctive configurations were studied.[44] The Fe cations of VNU-15 interact with each other along the same metal rod, called intra-chain interactions, and between neighboring metal rods (intermediated by linkers), called inter-chain interactions. The directions of these interactions are shown in Fig. 3(a). Eight high-spin Fe ions in the VNU-15 primitive cell can present up and down spins, resulting in 256 (2^8) spin configuration possibilities. Among the 256 spin

Table 1 Fe atom coordinates in relaxed DMA-1 and DMA-2 phases of VNU-15

Phase	Atom	Wyckoff position	Site symmetry	*x*	*y*	*z*
DMA-1	Fe1	16b	1	0.8283	0.0894	0.5818
	Fe2			0.5373	0.2938	0.6245
	Fe3			0.3264	0.5877	0.5836
	Fe4			0.1219	0.8788	0.5403
	Fe5			0.8312	0.5827	0.0884
	Fe6			0.8751	0.6255	0.2928
	Fe7			0.8329	0.5846	0.5867
	Fe8			0.7897	0.5413	0.8778
DMA-2	Fe1	16b	1	0.8307	0.0886	0.5837
	Fe2			0.5401	0.2918	0.6251
	Fe3			0.3273	0.5851	0.5869
	Fe4			0.1235	0.8764	0.5424
	Fe5			0.8276	0.5847	0.0876
	Fe6			0.8737	0.6261	0.2908
	Fe7			0.8314	0.5878	0.5841
	Fe8			0.7884	0.5433	0.8754

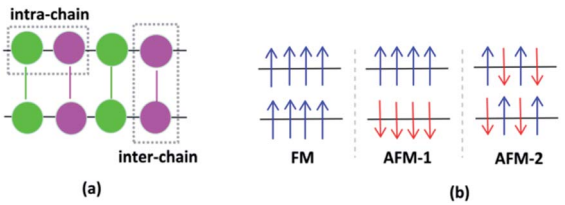

Fig. 3 (a) The intra-chain and inter-chain interactions between two chains of the primitive cell of VNU-15. The different magnetic configurations of VNU-15: (b) FM, (c) AFM-1, and (d) AFM-2 states, where the arrows indicate the spin directions of the Fe sites. Fe(1): green; Fe(2): pink; linker BDC^{2-}: green line; linker NDC^{2-}: pink line.

configurations that can occur in the primitive cell of VNU-15, we chose the three simplest configurations for consideration. First is the case where all Fe ions are of the same spin value, that is, all with spin up or spin down, as represented in Fig. 3(b). This state is the result of intra- and inter-chain ferromagnetic interactions, and is referred to as FM. The second state is the result of ferromagnetic intra-chain and antiferromagnetic inter-chain interactions, which is named AFM-1. The third occurs with Fe ions showing opposite spin values alternately along the rods, as well as opposite spin values between the adjacent rods of the VNU-15 channel. The latter state, designated as AFM-2, is the result of antiferromagnetic interactions both intra- and inter-chain.

Key crystal structure geometric parameters from the optimized structures of VNU-15 in the different magnetic states are listed in Table 2. The lattice parameters in this work are slightly different from those obtained from X-ray diffraction experiments, but the differences are in a reasonable range (the maximum relative lattice parameter error being smaller than 7.5%). This discrepancy comes from eliminating disorder in the simulated structure and from calculations being done at 0 K, while the experimental structure was obtained at room temperature (298 K). The DMA-2 phase has been found to have a more-negative total energy compared to the DMA-1 phase and, obviously, the DMA-2 phase is more stable than the DMA-1 phase. The lattice parameters of the DMA-1 and DMA-2 phases showed slight discrepancies, and the volume of the DMA-2 phase was smaller by about 0.3% than the DMA-1 phase.

Deviations from the experimentally predicted structures have been studied in more detail through analysis of bonding interactions. Fe(1) and Fe(2) octahedra are in 8b (D_{2h} symmetry) and 32 h (C_{2v} symmetry) sites with *Fddd* symmetry. After optimization, both octahedra were in 16b sites with *Fdd*2 symmetry. The optimized bonds agreed well with the published crystal structure at a level no worse than that corresponding to a deviation value of 0.20 Å. The different magnetic configurations affected the bond lengths by a tiny amount in the same phase. However, different DMA orientations resulted in different Fe–O(S) bond lengths in each phase. For instance, the Fe(1)–O(1S) bond length in the DMA-2 phase is shorter than that of the DMA-1 phase by 0.16 Å, whereas the Fe(2)–O(2S) length in the DMA-2 phase is longer than that in the DMA-1 phase by 0.21 Å. The Fe(1)–O(1C) bond is stronger than the Fe(1)–O(2C) bond because of its shorter bond length, similar to the Fe(2) case. The dissimilar strengths of the two BDC^{2-} and NDC^{2-} linkers result in the difference in bond length. To further describe the Fe–O chains, the super-exchange Fe(1)–O(2C)–Fe(2) angle and O(2C)–Fe–O(2C) angle were studied. The super-exchange angle of VNU-15 is about 107–108°, larger compared with that of Fe–MOF-74 (105.90°),[45] while the distance between two nearest Fe–Fe atoms is equal to 3.60 Å, which is larger than that of Fe–MOF-74 (2.90 Å). The O(2C)–Fe(1)–O(2C) angle is 180°, which leads to an Fe(2)–Fe(2) distance equal to two times that of the Fe(1)–Fe(2) distance. The O(2C)–Fe(2)–O(2C) angle is 57.49°, which leads to an Fe(1)–Fe(1) distance smaller than two times that of the Fe(1)–Fe(2) distance. The calculated super-exchange and O–Fe–O angles were found to be smaller than those from experiments, as shown in Table 2.

Structural analysis revealed that the SBUs were connected *via* four linker molecules, forming layers parallel to the (001) plane. Dispersion forces are important for capturing long-range

Table 2 The optimized lattice constants, bond lengths, and interlayer spacing (d) values of VNU-15 in one ferromagnetic (FM) and two anti-ferromagnetic (AFM-1 and AFM-2) configurations with relative errors in comparison to experimental values indicated in round brackets

		Experiment	Simulation					
			DMA-1			DMA-2		
			FM	AFM-1	AFM-2	FM	AFM-1	AFM-2
IT		70	43					
Crystal system		Orthorhombic						
Space group		*Fddd*	*Fdd*2					
Number of atoms per unit cell		1088	976					
Lattice constant	a (Å)	16.76	16.99 (+1.37%)	17.01 (+1.49%)	17.03 (+1.61%)	17.19 (+2.57%)	17.18 (+2.51%)	17.14 (+2.27%)
	b (Å)	18.83	17.80 (−5.49%)	17.79 (−5.52%)	17.75 (−5.74%)	17.42 (−7.49%)	17.43 (−7.43%)	17.53 (−6.90%)
	c (Å)	39.00	39.71 (+1.82%)	39.73 (+1.87%)	39.72 (+1.85%)	40.01 (+2.59%)	40.00 (+2.56%)	39.90 (+2.31%)
	V (Å3)	12 304.49	12 012.20 (−2.38%)	12 016.08 (−2.34%)	12 006.39 (−2.42%)	11 976.89 (−2.66%)	11 980.13 (−2.64%)	11 990.40 (−2.55%)
Bond length (Å)	Fe(1)–Fe(2)	3.60	3.51	3.51	3.51	3.48	3.48	3.49
	Fe(1)–Fe(1)	6.30	6.15	6.15	6.15	6.12	6.12	6.13
	Fe(2)–Fe(2)	7.21	7.02	7.02	7.02	6.97	6.97	6.99
	Fe(1)–O(1S)	2.12	2.16	2.16	2.16	2.00	2.00	1.99
	Fe(1)–O(1C)	2.03	2.05	2.05	2.04	2.02	2.02	2.02
	Fe(1)–O(2C)	2.17	2.10	2.10	2.10	2.05	2.05	2.05
	Fe(2)–O(2S)	2.09	1.97	1.97	1.97	2.18	2.18	2.17
	Fe(2)–O(1C)	2.09	1.97	1.97	1.97	2.02	2.02	2.02
	Fe(2)–O(2C)	2.26	2.24	2.24	2.24	2.23–2.34	2.24–2.33	2.22–2.34
	N–H⋯O–S (1)	1.90–196	1.74–1.77	1.74	1.74	1.80–1.83	180–1.83	1.80–1.82
	N–H⋯O–S (2)	—	—	—	—	1.74	1.70–1.74	1.71
Angle	Fe1–O_{C2}–Fe2	108.89	108.14	108.09	108.20	106.83	106.98	107.26
	O_{C2}–Fe_1–O_{C2}	180.00	178.01	177.92	178.08	178.67	178.70	179.12
	O_{C2}–Fe2–O_{C2}	57.49	58.48	58.47	58.60	57.42	57.42	57.51
Interlayer spacing d (Å)		3.40	3.39	3.38	3.38	3.36	3.36	3.36

Table 3 Exchange energy ($E_{ex} = E_{FM} - E_{AFM}$), and the total and local magnetic moments of the FM and AFM states in both phases of VNU-15

Phase	Magnetic model	Exchange energy (eV per primitive cell)	Fe magnetic moment (μ_B per atom)				Total magnetic moment (μ_B per primitive cell)
DMA-1	FM	0.010	3.793	4.282	3.793	4.282	36.0
			3.793	4.282	3.793	4.282	
	AFM-1	0.000	−3.793	−4.282	−3.793	−4.282	0.0
			3.793	4.282	3.793	4.282	
	AFM-2	0.020	3.776	−4.282	3.777	−4.282	0.0
			−3.776	4.282	−3.777	4.282	
DMA-2	FM	0.020	4.315	3.781	4.315	3.781	36.0
			4.315	3.781	4.315	3.781	
	AFM-1	0.018	−4.315	−3.781	−4.315	−3.781	0.0
			4.315	3.781	4.315	3.781	
	AFM-2	0.000	4.311	−3.773	4.311	−3.773	0.0
			−4.311	3.773	−4.311	3.773	

interactions, such as the π–π stacking of aromatic rings, which support the framework and are able to permanently sustain pores. Indeed, the distance between two adjacent layers predicted from the present calculations is about 3.37 Å, which is within the vdW interaction distance of 2D conjugated carbon layers, and the closest Fe distance between two layers is 3.50 Å, indicating strong vdW interactions and metal–metal interactions between the two layers, confirming the findings of a previous experimental paper.[26]

The relative energy per primitive cell can be used to identify the preferred magnetic coupling of VNU-15, as shown in Table 3. It was found that the AFM-1 state has the lowest total energy compared to the others and, thus, the AFM-1 state is the most stable for the DMA-1 phase, while the AFM-2 configuration is the most stable for the DMA-2 phase. It is clear that AFM ordering is the magnetic ground state of VNU-15. Meanwhile, the magnetic ground state of Fe–MOF-74 is FM ordering. This statement is explained based on the distance between adjacent Fe centers affecting the direct exchange interactions between them ($d_{Fe-Fe} = 2.90$ Å in Fe–MOF-74 and $d_{Fe-Fe} = 3.50$ Å in VNU-15). In all cases, there are two local magnetic moments of 3.80 μ_B and 4.30 μ_B per Fe ion, reflecting the different oxidation states of Fe(1) and Fe(2). Specifically, Fe(1) and Fe(2) hold values of 3.80 μ_B and 4.30 μ_B in the DMA-1 phase, respectively, but the opposite is true in the DMA-2 phase. The magnetic moment of the O atoms has a very small value of 0.10 μ_B, originating from the interactions of O atoms with neighboring Fe atoms.

The effect of magnetic anisotropy on the electronic structures and magnetic properties was assessed utilizing non-collinear spin calculations. The initial local magnetic moments for each Fe ion were given in different directions. The local magnetic moments of Fe ions are primarily assigned along the *z*-direction and give rise to small projected values in the *x*- and *y*-directions. In addition, the local magnetic moment of each Fe ion, *via* considering spin–orbit coupling, was found to be only 0.002 μ_B smaller than the values obtained in the isotropic case. Apparently, spin–orbit coupling was negligible in VNU-15. Consequently, non-collinear and spin–orbit coupling effects were not considered in the rest of the paper as the influence on the atomic magnetic moments is negligible.

In order to check whether long-range magnetic ordering exists in the framework, the spin densities of VNU-15 were calculated and plotted, as shown in Fig. 4. Positive (yellow color) spin densities allocated along each SBU direction were found in the FM state, as shown in Fig. 4(a) and (d). The AFM-1 configuration displayed negative (blue) and positive (yellow) spin densities distributed along each SBU direction, as shown in Fig. 4(b) and (e). Meanwhile, adjacent blue and yellow spin densities distributed along the same chain were presented in the AFM-2 model, as shown in Fig. 4(c) and (f). As can be seen in Fig. 4, the magnetization is utterly localized on the Fe–O chains, resulting in tiny amounts of inter-chain coupling.

B. Electronic structures and charges

The spin-polarized electronic band structures were calculated using the GGA+U method for the AFM configurations between the high-symmetry points of the first Brillouin zone (Fig. 5(a)), as shown in Fig. 5(b) and (c). The band gaps of the DMA-1 and DMA-2 phases were 1.28 eV and 1.13 eV, respectively, indicating that VNU-15 belongs to the semiconductor class. Apparently, the reorientation of DMA cations led to the DMA-2 phase showing a narrower band gap than the DMA-1 phase and also a more disperse band structure. The AFM-1 valence band minimum (VBM) and conduction band maximum (CBM) of the

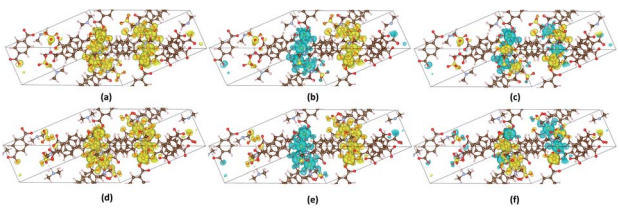

Fig. 4 Three-dimensional spin density ($\rho\uparrow - \rho\downarrow$) with the isosurface at 2×10^{-3} e Å^{-3} for the VNU-15 primitive cell for the (a) FM, (b) AFM-1, and (c) AFM-2 models of the DMA-1 phase and the (d) FM, (e) AFM-1, and (f) AFM-2 models in the DMA-2 phase. Positive and negative spin densities are denoted by yellow and blue, respectively.

DMA-1 phase were at the Z(0, 0, 0.5) and G(0, 0, 0) points, respectively. The AFM-2 VBM and CBM of the DMA-2 phase were at the S(−0.5, 0.5, 0) point. The electronic band structures for all

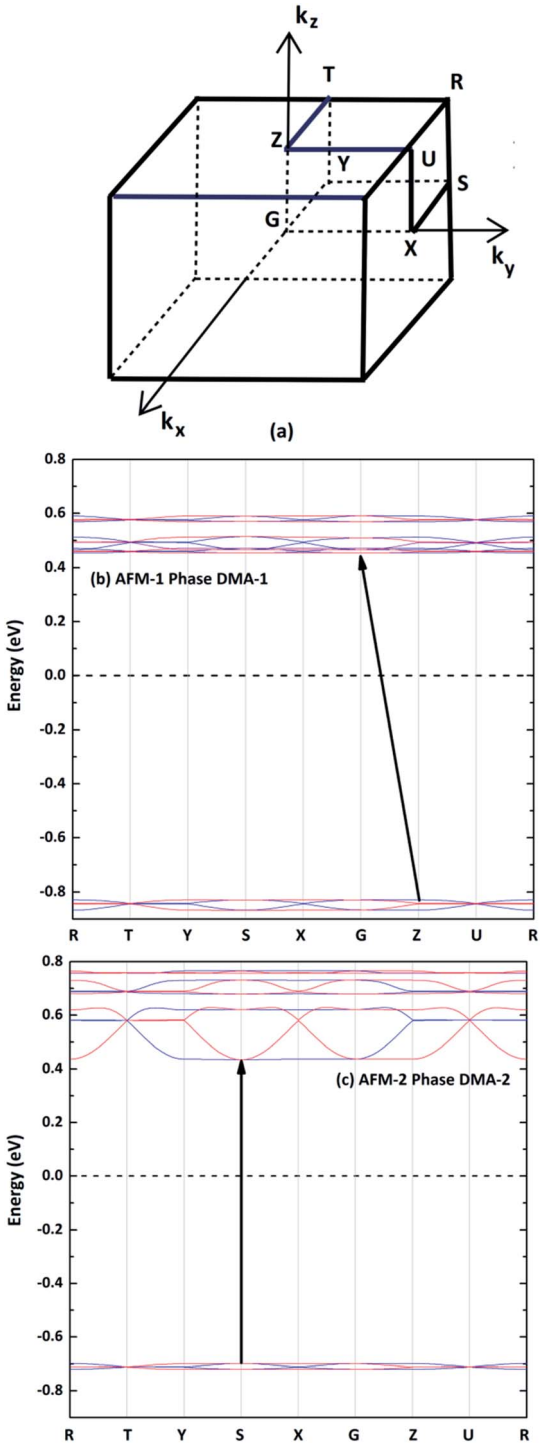

Fig. 5 (a) High-symmetry points in the first Brillouin zone for the orthorhombic crystal. The band structures of (b) AFM-1 of the DMA-1 phase and (c) AFM-2 of the DMA-2 phase, where the blue and red lines represent up- and down-spins, respectively. The dotted lines represent the Fermi level. High symmetry points: S(−0.5, 0.5, 0), X(0, 0.5, 0), U(0, 0.5, 0.5), R(−0.5, 0.5, 0.5), G(0, 0, 0), Z(0, 0, 0.5), T(−0.5, 0, 0.5), and Y(−0.5, 0, 0).

magnetic configurations of the VNU-15 structure are depicted in Fig. S1, ESI.†

To further understand the nature of the band structure, the total DOS of VNU-15 and partial DOS of ions around the Fermi energy E_F were examined, as displayed in Fig. 6. The valence and conduction bands of DMA-1 show mainly Fe(1) and Fe(2) 3d-orbital contributions, respectively, whereas the situation is opposite for DMA-2. The low-lying band (below the valence band) is mainly centered on the orbitals of SO_4^{2-} ions in both phases. The spin-polarized TDOS clearly displays nearly symmetric features in the spin-up and spin-down states of the AFM configurations. The electronic structures were found to be strongly influenced by on-site Coulomb repulsion. This breaks the strong Fe 3d–O 2p hybridization observed in the electronic structure calculated using the GGA (see Fig. S3, ESI†), resulting in the occupied Fe 3d states being shifted to higher energies. In contrast to the GGA, which predicts VNU-15 to be half-metal, GGA+U leads to a charge-transfer-type d–d gap of nearly 1.20 eV. It is reported that the GGA underestimates the band gap because it inadequately describes the strong correlation effect between 3d electrons localized on metal ions.[29] Although there is no experimental band gap for reference, the band gap of Fe–MOF-74 was utilized for comparison. Fe–MOF-74 has a band gap of 0.30 eV, with a nearest Fe–Fe distance of 2.90 Å. Therefore, the band gap of VNU-15 may be roughly 1.20 eV with a distance of 3.50 Å. Consequently, the band gap obtained from GGA+U is more reasonable than that obtained *via* the GGA.[17]

The LDOS for two adjacent Fe(1) and Fe(2) ions with reverse spins and different m_l values are presented in Fig. 7 to clarify the oxidation states. It turns out that the spin-down components relocate to a much higher energy than the spin-up ones. Fe^{2+} has d^6 configuration and four unpaired d electrons, while Fe^{3+} has d^5 configuration and five unpaired d electrons. Fig. 7(a) and (b) show that there are four and five unpaired d electrons from Fe(1) and Fe(2), respectively, in the DMA-1 phase. Fig. 7(c) and (d) show that there are five and four unpaired d electrons for Fe(1) and Fe(2), respectively, in the DMA-2 phase. It was predicted that the oxidation states of Fe(1) and Fe(2) were +2 and +3 in the DMA-1 phase, whereas the oxidation states of Fe(1) and Fe(2) were +3 and +2 in DMA-2. These findings are supported based on the magnetic moments in Table 2 and Bader charges in Table 4. Specifically, the calculated Fe(1) and Fe(2) magnetic moments were 3.80 μ_B and 4.30 μ_B for the DMA-1 phase and, reversely, these values were 4.30 μ_B and 3.80 μ_B for the DMA-2 phase. The calculated Fe(1) and Fe(2) charges were found to be 1.80$|e|$ and 1.48$|e|$ for the DMA-1 phase, however, these charges were 1.45$|e|$ and 1.86$|e|$ for the DMA-2 phase.

From Table 4, the average charges show insignificant variations between the spin configurations in the same phase. O(2C) has similar charges to O(1C) in both phases. The change in the orientation of DMA caused S to increase by 0.02$|e|$ in the DMA-2 phase. In addition, it also changed the charges of O(1S) and O(2S) in the two phases. The charges of O(1S) and O(2S) in DMA-1 were −1.33$|e|$ and −1.26$|e|$, and these changed to −1.28$|e|$ and −1.33$|e|$ in the DMA-2 phase. The charge of O(3S) underwent a negligible change in the two cases. The charges of the atoms in the linker are very small, indicating the vdW

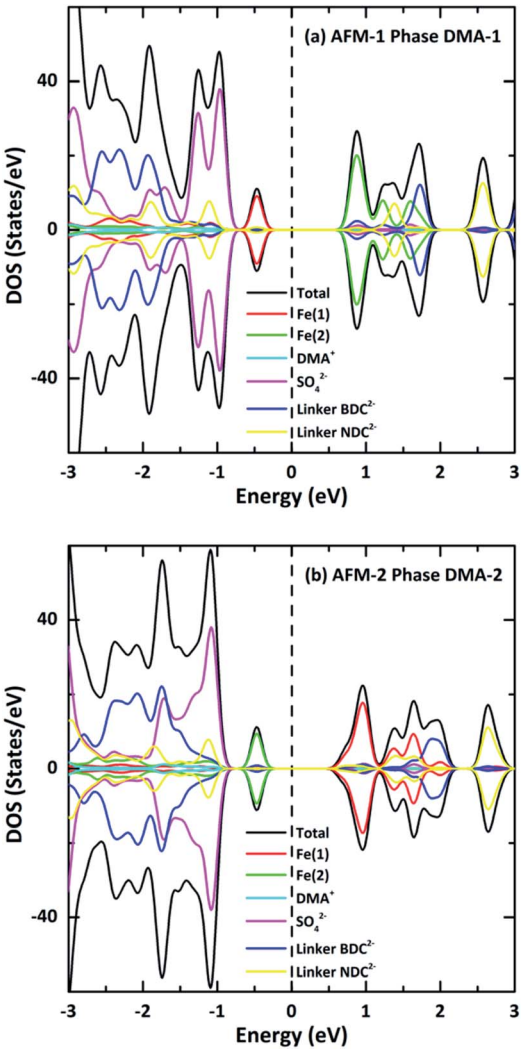

Fig. 6 Total and partial densities of state of (a) AFM-1 of the DMA-1 phase and (b) AFM-2 of the DMA-2 phase of VNU-15. The tops and bottoms of each part of the figure represent the spin-polarized DOS for the up and down spin orientations, respectively, and the dotted lines show the Fermi energy.

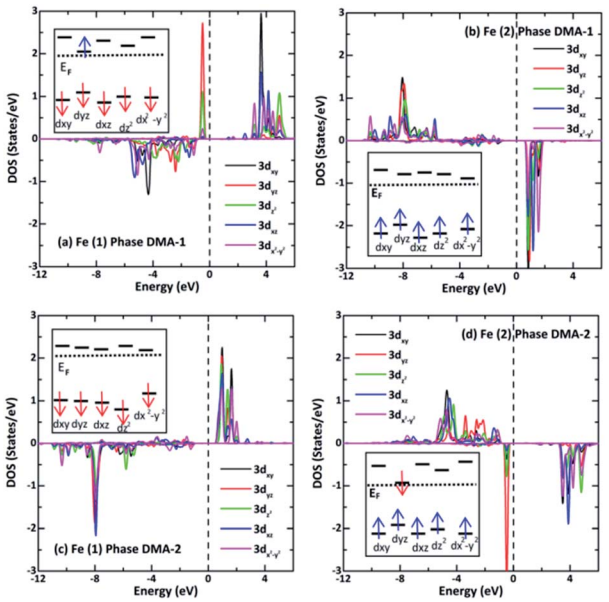

Fig. 7 Spin-resolved LDOS (a and c) for Fe(1) and (b and d) for Fe(2) 3d projected orbitals in the AFM-2 configuration of the DMA-1 and DMA-2 phases of VNU-15, respectively. The electron-spin polarized configurations arranged in the high-spin states for Fe $3d^6$ and Fe $3d^5$ are systematically illustrated in the inset.

interactions between the linkers. Furthermore, only the charges of O atoms are found to be negative, while the other atom charges are positive, reflecting the ionic bonds between the atoms.

GGA+U calculations of the charge density difference were executed to clarify the nature of chemical bonding in VNU-15, as shown in Fig. 8. For BDC^{2-} and NDC^{2-} linkers, the plot shows that charge is mainly concentrated on the hydrogen atoms, and the charge transfer effect is insignificant. This can be explained by the fact that the stacked layers along the *z*-direction in the VNU-15 structure are held together by vdW interactions, which in turn is consistent with the analysis in the above discussion. For the SBUs, electrons transferring from O to Fe, C, and S sites indicates that Fe–O, C–O, and S–O bonding is ionic. Moreover, there are remarkable ionic bonds between Fe 3d–O 2p states, which stabilizes the structure. The findings relating to the nature of chemical bonding from GGA+U are similar to those from the GGA.

C. Photocatalytic activity

Because the band gap is small, VNU-15 is capable of absorbing infrared light, and we expect that VNU-15 can be used in the photocatalytic field. In order to prove the possibility of VNU-15 acting as a photocatalyst, the reduction and oxidation potentials of the CB and VB edges can be calculated as follows:

$$E_{VB} = \chi - E^e + \frac{1}{2}E_g, \quad (4)$$

Table 4 Bader charges (|*e*|) for the different magnetic configurations of VNU-15 in both phases

	DMA-1 phase			DMA-2 phase		
Atom/state	FM	AFM-1	AFM-2	FM	AFM-1	AFM-2
Fe(1)	1.804	1.804	1.805	1.445	1.445	1.446
Fe(2)	1.482	1.482	1.479	1.859	1.859	1.857
O(1C)	−1.116	−1.116	−1.117	−1.116	−1.117	−1.117
O(2C)	−1.139	−1.139	−1.136	−1.147	−1.146	−1.143
O(1S)	−1.334	−1.334	−1.333	−1.287	−1.286	−1.286
O(2S)	−1.263	−1.263	−1.263	−1.328	−1.328	−1.327
O(3S)	−1.315	−1.316	−1.315	−1.319	−1.320	−1.319
C(1)	0.353	0.353	0.356	0.344	0.344	0.343
C(2)	0.215	0.215	0.213	0.227	0.226	0.228
S	3.712	3.713	3.711	3.733	3.734	3.733
H(linker)	0.097	0.096	0.094	0.098	0.099	0.098
DMA^+	0.470	0.466	0.459	0.421	0.422	0.432
SO_4^{2-}	−1.515	−1.515	−1.515	−1.518	−1.520	−1.518

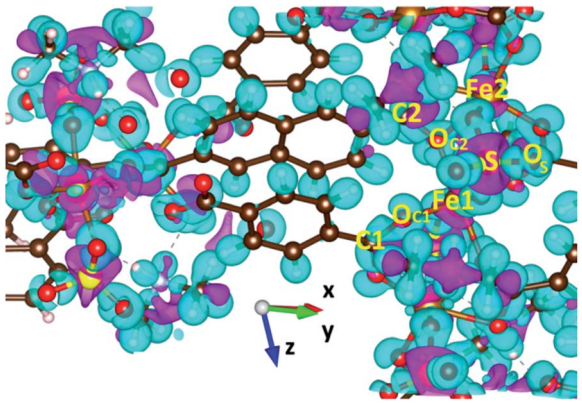

Fig. 8 The charge density difference of AFM-2 of the DMA-2 phase of VNU-15. An isosurface value of 0.02 e Å^{-3} is shown in the colored region. The positive and negative charge densities are denoted by pink and cyan, respectively.

$$E_{CB} = E_{VB} - E_g, \quad (5)$$

where E_{CB} and E_{VB} are, respectively, the potentials of the CB and VB edges, E^e is the standard electrode potential on the hydrogen scale (*ca.* 4.44 eV), and E_g is the band gap of the semiconductor.[46]

χ is the electronegativity of the semiconductor calculated as the geometric mean of the absolute electronegativities of the constituent atoms, $x(A)$:

$$\chi = \sqrt[N]{x(A)^a x(B)^b \ldots x(C)^c}, \quad (6)$$

where a and N are the number of species and total number of atoms in the compound, respectively. The electronegativity of a constituent atom is the arithmetic mean of the atomic electron affinity, E_{EA}, and the first ionization energy, E_{FIE}:[47]

$$x = \frac{1}{2}|E_{EA} + E_{FIE}|. \quad (7)$$

The calculated electronegativity of VNU-15 is 6.79 eV. Therefore, the calculated oxidation and reduction potentials of the VB and CB edges are 2.85 V and 1.72 V, respectively, as shown in Fig. 9. O_2 is not reduced to $O_2^{\bullet-}$ by the photogenerated electrons in the CB of VNU-15. The VB potential of VNU-15 is more positive than the oxidation potentials of H_2O_2/H_2O (1.77 V), O_3/H_2O (2.07 V), and $^{\bullet}OH/H_2O$ (2.27 V).[48] Therefore, the photogenerated holes can oxidize H_2O to produce the active species H_2O_2, O_3, and $^{\bullet}OH$, which can further decompose dye molecules and organic pollutants.

High mobility indicates fast carrier transport speeds from the bulk to the surface. This can diminish the electron–hole recombination probability within a semiconductor and strengthen the photocatalytic activity. The mobility of photogenerated electrons and holes has been investigated in a previous study.[49] Based on a nearly free electron approximation, the mobility of photoexcited carriers can be calculated *via* the following formula:

$$v = \frac{\hbar k}{m^*}, \quad (8)$$

where ħ is the reduced Planck constant, k is the wavevector, and m^* is the effective mass of electrons or holes (a 3 × 3 tensor matrix).[48] It is worth mentioning that eqn (8) may not be valid for the strongly correlated electron system investigated in this work. To assess the mobility of carriers, the effective mass tensors of carriers should be calculated by taking into account the anisotropic properties of the electronic structure at extreme k-points, as follows:

$$m_{ij}^* = \pm\hbar^2\left(\frac{\partial^2 E}{\partial k_i \partial k_j}\right)^{-1}, \quad (9)$$

where E is the band-edge energy. The effective masses of electrons (m_e^*) and holes (m_h^*) correspond to the positive and negative signs, respectively. Commonly, a larger effective mass implies lower migration ability and a higher recombination probability for carriers within the semiconductor. Carriers in flat and disperse bands have large and small effective masses, respectively. Because the band structure of the DMA-2 phase is more dispersed than that of the DMA-1 phase, in this section, we only focus on a discussion of the DMA-2 phase. The masses were gained by fitting parabolic functions within an energy difference of 5 meV around the VBM and CBM along the designated directions. The 3D band structures for carrying out this calculation are shown in Fig. S4† (ESI), and the effective mass results are summarized in Table 5.

In order to achieve good photocatalytic performance, the difference between the electron and hole effective masses should be large, to reduce the rate of recombination. Moreover, the effective hole mass should be smaller than the electron mass in order to move quickly to the surface, because only holes are involved in the photocatalytic process. In the spin-up case, the effective hole mass is lighter than the electron mass along the [100], [010], and [0$\bar{1}$1] directions, whereas the ratio between m_e^* and m_h^* along the [0$\bar{1}$1] direction is greater than in the two remaining directions. For the spin-down case, the effective hole

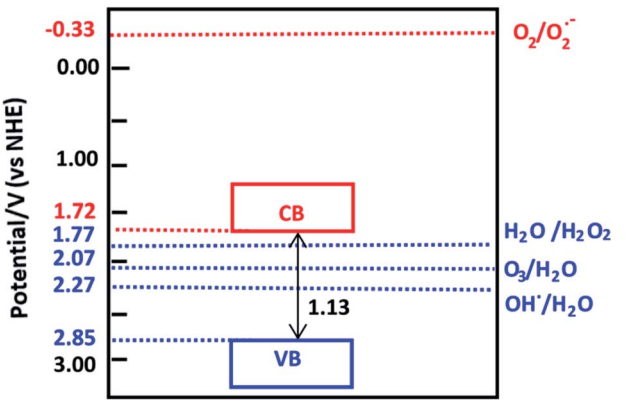

Fig. 9 The reduction and oxidation potentials of the CB and VB edges of VNU-15. The oxidation potential of $O_2/O_2^{\bullet-}$ is −0.33 V and the reduction potentials of H_2O/H_2O_2, O_3/H_2O, and $^{\bullet}OH/H_2O$ are 1.77 V, 2.07 V, and 2.27 V, respectively.

Table 5 Effective electron (m_e^*) and hole (m_h^*) masses in free-electron mass units for AFM-2 of the DMA-2 phase of VNU-15 from GGA+U calculations

	Direction					
	[100]	[010]	[001]	[1$\bar{1}$0]	[0$\bar{1}$1]	[1$\bar{1}$1]
$m_h^*(\uparrow)$	0.368	0.366	11.564	0.089	0.094	0.328
$m_e^*(\uparrow)$	1.720	1.724	0.037	0.034	0.617	0.035
$m_h^*(\downarrow)$	11.406	11.564	0.366	0.304	18.503	0.327
$m_e^*(\downarrow)$	0.037	0.037	1.723	0.009	0.009	0.035

mass is lighter than the electron mass along the [001] direction, and the ratio between the electron and hole effective masses is around 5. Therefore, it can be predicted that the photocatalytic activity on the surfaces corresponding to the [0$\bar{1}$1] and [001] directions is efficient in the spin-up and spin-down cases, respectively.

The 3D band structures can qualitatively demonstrate the effective mass in the plane rather than special cases.[50] For instance, the 3D band structures for the valence and conduction bands in the k_y–k_z plane are depicted in Fig. 10, where the chosen k-points are all centered at the S point. Fig. 10(a) and (c) exhibit that the projections of the valence bands are flat ellipses, hence, the effective hole masses are strongly anisotropic. Because of the much longer axis of the flat ellipse, the effective mass of photogenerated holes in the spin-up case is much larger along the [001] direction compared to the [010] direction. Meanwhile, the effective photogenerated hole mass for spin down is larger along the [010] direction compared to the [001] one. Similarly, Fig. 10(b) and (d) show that the projections of the conduction bands are flat ellipses, hence, the effective electron masses show significant differences in different directions. These findings are very supportive of the data shown in Table 5.

The theoretical findings in this paper can be validated by experiments in different ways. Firstly, DMA-2 formation can be detected by electric control of the orientation of H-bonding between the DMA^+ molecules and the framework using second-harmonic generation techniques.[30,51] The DMA^+ band-structure effect could be probed using angular-resolved photoelectron spectroscopy. It is possible to study the effectiveness of VNU-15 in photocatalysis *via* adding its powder to RhB or TC-H solution. The suspension is stirred for a given time interval in a dark environment to reach adsorption–desorption equilibrium. After infrared light illumination, which is generated using a Xe lamp with a suitable filter, the suspension is collected after a given period of time and separated *via* centrifugation. This approach was used for mixed-valence Fe^{II}/Fe^{III} Fe–MIL-53.[52] Secondly, ac impedance measurements can be performed using a pelletized sample of VNU-15 in a magnetic field from low relative humidity to medium humidity at an elevated temperature. This experiment can be used to check how the intrinsic magnetic properties predicted in this work would affect the proton transport properties of VNU-15 with respect to an applied magnetic field.

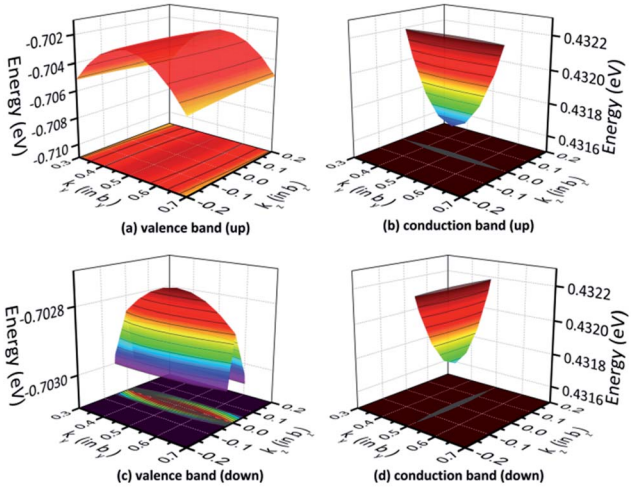

Fig. 10 The band structure for AFM-2 of the DMA-2 phase in the k_y–k_z plane with the (a) valence and (b) conduction bands for spin up, and the (c) valence and (d) conduction bands for spin down.

IV. Conclusions

A detailed investigation into the electronic structures, magnetic properties, and bonding natures of VNU-15 with two different DMA cation orientations using linear response DFT+U methods has been presented. The calculations show that VNU-15 still retains an orthorhombic crystal structure after eliminating structural disorder. Our results imply a possible new phase of VNU-15 with another DMA cation orientation in the pores. Based on the linear response method, the Hubbard U term acting on the 3d sites of Fe was determined to be 4.30 eV. Density of states studies reveal that VNU-15 shows semiconductor behavior with a band gap of approximately 1.20 eV. The calculated magnetic moments show that VNU-15 is an antiferromagnetic system at a temperature of 0 K, with values of 3.80 μ_B and 4.30 μ_B for each different Fe atom. The valence band and conduction band of VNU-15 are mainly composed of Fe 3d states. The change in the orientation of DMA^+ led to changes in the dispersion of the band structure, the band gap, and the Fe contributions to the valence band and conduction band. Such an effect could be used for spin-control in porous and molecular magnets. Charge density difference analysis consistently supports the notion that the bonding interactions between Fe–O, S–O, and C–O mainly involve ionic interactions, whereas those between ligands mainly involve van der Waals interactions. The inclusion of Hubbard correlation effects significantly improves the band gap and magnetic moment predictions for VNU-15. This strongly points to the importance of correlation for studying the physics of iron-based MOFs. The VBM potential of VNU-15 is 2.85 V and the CBM potential is 1.72 V, indicating that the photogenerated holes have strong oxidation abilities. Additionally, the separation and transfer of photogenerated carriers along the [0$\bar{1}$1] and [001] directions for spin up and down, respectively, are more effective compared with other directions based on analysis of the effective masses. These

theoretical results suggest a wide range of applications for VNU-15 in photocatalysis, and investigations into the proton transport properties of magnetic MOF materials would be an interesting subject for future studies.

Conflicts of interest

There are no conflicts to declare.

Author contributions

D. T.-X. D. and D. N.-M. designed the study and wrote and edited the main draft. D. T.-X. D. and H. C. D. performed the computational works. D. T.-X. D. analyzed data and figures and carried out administrative duties relating to the project. D. N.-M. supervised tasks. Y. K. and J.-L. K. provided computational resources and software. All authors discussed the results and commented on the manuscript.

Acknowledgements

The work was supported by grants from Vietnam National University Ho Chi Minh City grant number B2018-50-01. The authors express their sincere thanks to the staff of CCMS of the Institute for Materials Research, Tohoku University, for their continuous support and help in using the MASAMUNE-IMR, CRAY-XC50 supercomputing facilities. D. T.-X. D. thanks Mr Dai-Nam Le (Ton Duc Thang University, Vietnam) for his valuable comments. The authors thank two referees for their constructive and valuable suggestions.

Notes and references

1 H. Furukawa, K. E. Cordova, M. O'Keeffe and O. M. Yaghi, *Science*, 2013, **341**, 1230444.
2 L. H. T. Nguyen, T. T. Nguyen, H. L. Nguyen, T. L. H. Doan and P. H. Tran, *Catal. Sci. Technol.*, 2017, **7**, 4346.
3 P. T. K. Nguyen, H. T. D. Nguyen, H. N. Nguyen, C. A. Trickett, Q. T. Ton, E. Gutierrez-Puebla, M. Angeles Monge, K. E. Cordova and F. Gandara, *ACS Appl. Mater. Interfaces*, 2018, **10**, 733.
4 T. L. H. Doan, H. L. Nguyen, H. Q. Pham, N.-N. Pham-Tran, T. N. Le and K. E. Cordova, *Chem.–Asian J.*, 2015, **10**, 2660.
5 H. L. Nguyen, T. T. Vu, D. Le, T. L. H. Doan, V. Q. Nguyen and N. T. S. Phan, *ACS Catal.*, 2017, **7**, 338.
6 P. T. K. Nguyen, H. T. D. Nguyen, H. Q. Pham, J. Kim, K. E. Cordova and H. Furukawa, *Inorg. Chem.*, 2015, **54**, 10065.
7 H. T. D. Nguyen, Y. B. N. Tran, H. N. Nguyen, T. C. Nguyen, F. Gándara and P. T. K. Nguyen, *Inorg. Chem.*, 2018, **57**, 13772.
8 P. Horcajada, C. Serre, M. Vallet-Regi, M. Sebban, F. Taulelle and G. Ferey, *Angew. Chem.*, 2006, **45**, 5974.
9 S. R. Miller, D. Heurtaux, T. Baati, P. Horcajada, J.-M. Greneache and C. Serre, *Chem. Commun.*, 2010, **46**, 4526.
10 T. H. N. Lo, M. V. Nguyen and T. N. Tu, *Inorg. Chem. Front.*, 2017, **4**, 1509.
11 M. V. Nguyen, T. H. N. Lo, L. C. Luu, H. T. T. Nguyen and T. N. Tu, *J. Mater. Chem. A*, 2018, **6**, 1816.
12 N. L. Rosi, M. Eddaoudi, J. Kim, M. O'Keeffe and O. M. Yaghi, *Angew. Chem., Int. Ed.*, 2002, **41**, 284.
13 S. Horike, S. Shimomura and S. Kitagawa, *Nat. Chem.*, 2009, **1**, 695.
14 P. Horcajada, F. Salles, S. Wuttke, T. Devic, D. Heurtaux, G. Maurin, A. Vimont, M. Daturi, O. David, E. Magnier, N. Stock, Y. Filinchuk, D. Popov, C. Riekel, G. Ferey and C. Serre, *J. Am. Chem. Soc.*, 2011, **133**, 17839.
15 H. Deng, S. Grunder, K. E. Cordova, C. Valente, H. Furukawa, M. Hmadeh, F. Gándara, A. C. Whalley, Z. Liu, S. Asahina, H. Kazumori, M. O'Keeffe, O. Terasaki, J. F. Stoddart and O. M. Yaghi, *Science*, 2012, **336**, 1018.
16 C. Serre, F. Millange, C. Thouvenot, M. Nogues, G. Marsolier, D. Louer and G. Ferey, *J. Am. Chem. Soc.*, 2002, **124**, 13519.
17 Q. Zhang, B. Li and L. Chen, *Inorg. Chem.*, 2013, **52**, 9356.
18 J. Park, H. Kim and Y. Jung, *J. Phys. Chem. Lett.*, 2013, **4**, 2530.
19 D. Yu, A. O. Yazaydin, J. R. Lane, P. D. C. Dietzel and R. Q. Snurr, *Chem. Sci.*, 2013, **4**, 3544.
20 P. Canepa, Y. J. Chabal and T. Thonhauser, *Phys. Rev. B: Condens. Matter Mater. Phys.*, 2013, **87**, 094407.
21 S. Ling and B. Slater, *J. Phys. Chem. C*, 2015, **119**, 16667.
22 C. Combelles, M. B. Yahia, L. Pedesseau and M.-L. Doublet, *J. Power Sources*, 2011, **196**, 3426.
23 M. B. Gawande, P. S. Branco and R. S. Varma, *Chem. Soc. Rev.*, 2013, **42**, 3371.
24 C. Mathoniere, C. J. Nuttall, S. G. Carling and P. Day, *Inorg. Chem.*, 1996, **35**, 1201.
25 J.-P. Zhao, B.-W. Hu, F. Lloret, J. Tao, Q. Yang, X.-F. Zhang and X.-H. Bu, *Inorg. Chem.*, 2010, **49**, 10390.
26 T. N. Tu, N. Q. Phan, T. T. Vu, H. L. Nguyen, K. E. Cordova and H. Furukawa, *J. Mater. Chem. A*, 2016, **4**, 3638.
27 A. Shigematsu, T. Yamada and H. Kitagawa, *J. Am. Chem. Soc.*, 2011, **133**, 2034.
28 L.-M. Yang, P. Vajeeston, P. Ravindran, H. Fjellvag and M. Tilset, *Inorg. Chem.*, 2010, **49**, 10283.
29 D. T.-X. Dang, H. T.-D. Nguyen, N. Thoai, J.-L. Kuo, N. T. T. Nguyen and D. Nguyen-Manh, *Phys. Chem. Chem. Phys.*, 2020, **22**, 1598.
30 P. Jain, A. Stroppa, D. Nabok, A. Marino, A. Rubano, D. Paparo, M. Matsubara, H. Nakotte, M. Fiebig, S. Picozzi, E. S. Choi, A. K. Cheetham, C. Draxl, N. S. Dalal and V. S. Zapf, *npj Quantum Mater.*, 2016, **1**, 16012.
31 G. Kresse and J. Furthmuller, *Comput. Mater. Sci.*, 1996, **6**, 15.
32 G. Kresse and J. Furthmuller, *Phys. Rev. B: Condens. Matter Mater. Phys.*, 1996, **54**, 11169.
33 P. E. Blochl, *Phys. Rev. B: Condens. Matter Mater. Phys.*, 1994, **50**, 17953.
34 G. Kresse and D. Joubert, *Phys. Rev. B: Condens. Matter Mater. Phys.*, 1999, **59**, 1758.
35 J. P. Perdew, K. Burke and M. Ernzerhof, *Phys. Rev. Lett.*, 1996, **77**, 3865.
36 S. Grimme, S. Ehrlich and J. Goerigk, *J. Comput. Chem.*, 2011, **32**, 1456.

37 W. Tang, E. Sanville and G. Henkelman, *J. Phys.: Condens. Matter*, 2009, **21**, 084204.
38 K. Momma and F. Izumi, *J. Appl. Crystallogr.*, 2011, **44**, 1272.
39 S. L. Dudarev, G. A. Botton, S. Y. Savarsov, C. J. Humphreys and A. P. Sutton, *Phys. Rev. B: Condens. Matter Mater. Phys.*, 1998, **57**, 1505.
40 M. Cococcioni and S. D. Gironcoli, *Phys. Rev. B: Condens. Matter Mater. Phys.*, 2005, **71**, 035105.
41 H. M. Le, T.-T. Pham, T. S. Dinh, Y. Kawazoe and D. Nguyen-Manh, *J. Phys.: Condens. Matter*, 2016, **28**, 135301.
42 H. Li, M. Huang and G. Cao, *J. Mater. Chem. C*, 2017, **5**, 4557.
43 R. Hu, Y. H. Li, Z. H. Zhang, Z. Q. Fan and L. Sun, *J. Mater. Chem. C*, 2019, **7**, 7745.
44 M. Hosseini, D. E. P. Vanpoucke, P. Giannozzi, M. Berahman and N. Hadipour, *RSC Adv.*, 2020, **10**, 4786.
45 A. M. P. Moeljadi, R. Schmid and H. Hirao, *Can. J. Chem.*, 2016, **94**, 1144.
46 Y. Xu and M. A. A. Schoonen, *Am. Mineral.*, 2000, **85**, 543.
47 R. S. Mulliken, *J. Chem. Phys.*, 1934, **2**, 782.
48 J. Zhang, W. Yu, J. Liu and B. Liu, *Appl. Surf. Sci.*, 2015, **358**, 457.
49 H. Q. Pham, D. Q. Le, N.-N. Pham-Tran, Y. Kawazoe and D. Nguyen-Manh, *RSC Adv.*, 2019, **9**, 29440.
50 Z. Li, Y. Dai, X. Ma, Y. Zhu and B. Huang, *Phys. Chem. Chem. Phys.*, 2014, **16**, 3267.
51 Y. Tian, J. Cong, S. Shen, Y. Chai, L. Yan, S. Wang and Y. Sun, *Phys. Status Solidi RRL*, 2014, **8**, 91.
52 H. Chen, Y. Liu, T. Cai, W. Dong, L. Tang, X. Xia, L. Wang and T. Li, *ACS Appl. Mater. Interfaces*, 2019, **11**, 28791.